Criteria for Dynamical Timescale Mass Transfer of Metal-poor Intermediate-mass Stars

Hongwei Ge[1,2,3] ⓘ, Christopher A Tout[2] ⓘ, Xuefei Chen[1,3] ⓘ, Arnab Sarkar[2] ⓘ, Dominic J Walton[4] ⓘ, and Zhanwen Han[1,3,5] ⓘ

[1] Yunnan Observatories, Chinese Academy of Sciences, 396 YangFangWang, Guandu District, Kunming, 650216, People's Republic of China; gehw@ynao.ac.cn,
cxf@ynao.ac.cn, zhanwenhan@ynao.ac.cn
[2] Institute of Astronomy, The Observatories, University of Cambridge, Madingley Road, Cambridge, CB3 0HA, UK; cat@ast.cam.ac.uk, as3158@cam.ac.uk
[3] Key Laboratory for Structure and Evolution of Celestial Objects, Chinese Academy of Sciences, P.O. Box 110, Kunming 650216, People's Republic of China
[4] Centre for Astrophysics Research, University of Hertfordshire, College Lane, Hatfield, AL10 9AB, UK; dwalton354@gmail.com
[5] University of Chinese Academy of Sciences, Beijing 100049, People's Republic of China

Abstract

The stability criteria of rapid mass transfer and common-envelope evolution are fundamental in binary star evolution. They determine the mass, mass ratio, and orbital distribution of many important systems, such as X-ray binaries, type Ia supernovae, and merging gravitational-wave sources. We use our adiabatic mass-loss model to systematically survey intermediate-mass (IM) stars' thresholds for dynamical timescale mass transfer. The impact of metallicity on the stellar responses and critical mass ratios is explored. Both tables ($Z = 0.001$) and fitting formulae ($Z = 0.001$ and $Z = 0.02$) of the critical mass ratios of IM stars are provided. An application of our results to intermediate-mass X-ray binaries (IMXBs) is discussed. We find that the predicted upper limit to mass ratios, as a function of orbital period, is consistent with the observed IMXBs that undergo thermal or nuclear timescale mass transfer. According to the observed peak X-ray luminosity, L_X, we predict the range of L_X for IMXBs as a function of the donor mass and the mass-transfer timescale.

Unified Astronomy Thesaurus concepts: Binary stars (154); Stellar evolution (1599); Stellar physics (1621); Common envelope evolution (2154); X-ray binary stars (1811)

Supporting material: machine-readable table

1. Introduction

The fraction of binaries including multiple stars is over half of all stellar systems (e.g., Duchêne & Kraus 2013; Moe & Di Stefano 2017; Li et al. 2022), and it can be even up to 70% for massive stars (Sana et al. 2012). The evolution of close binary stars can form X-ray binaries, pulsar binaries, type Ia supernovae, white dwarf/neutron star (NS)/stellar-mass black hole (BH) binaries, etc. The stability of rapid mass transfer and the common-envelope evolution (Paczynski 1976) are fundamental problems in binary evolution and determine the fate of binary systems. Recent studies (Ge et al. 2015; Pavlovskii et al. 2017; Ge et al. 2020a; Marchant et al. 2021; Temmink et al. 2023) suggest that the critical initial mass ratios for dynamical timescale mass transfer are larger than previously expected from polytropic stellar models, with the exception of massive early main-sequence (MS) stars (Ge et al. 2015, 2020a). So, binaries in a stable mass-transfer channel contribute significantly to merging BHs (e.g., Inayoshi et al. 2017; Gallegos-Garcia et al. 2021; Briel et al. 2022; Dorozsmai & Toonen 2022).

Specifically, intermediate-mass X-ray binaries (IMXBs) are important and energetic objects among binary systems with donor masses $1.5 < M/M_\odot < 10.0$. They are rare and little studied previously compared with low- and high-mass X-ray binaries. However, for the current low-mass X-ray binary (LMXB) Cygnus X-2, King & Ritter (1999) and Podsiadlowski & Rappaport (2000) independently suggest the luminous and hot companion ($M \approx 0.5\ M_\odot$) formed through nonconserved and super-Eddington thermal timescale mass transfer from a previous $M \approx 3.5\ M_\odot$ star. Tauris et al. (2000) provide a detailed calculation of IMXBs with 2–6 $M_\odot$ donors and 1.3 $M_\odot$ accretors and demonstrate that in many cases systems will evolve to binary millisecond pulsars. Podsiadlowski et al. (2002) present systematically the evolution of I/LMXBs with 0.6–7 $M_\odot$ donors. Shao & Li (2012) further present a systematic study of I/LMXBs with different NS masses. Misra et al. (2020) show that observed super-Eddington luminosities can be achieved in I/LMXBs undergoing a nonconserved mass transfer. Clearly, the upper limit of the initial mass ratio ($q = M_{\rm donor}/M_{\rm accretor}$) to form I/LMXBs should be, in principle, consistent with the critical initial mass ratio for dynamical timescale mass transfer. The allowed parameter space of the initial orbital periods and donor masses from the above studies suggests the critical initial mass ratio $q \approx 3$–4 for dynamical timescale mass transfer of radiative donor stars. This is in agreement with studies by Hjellming (1989) and Kalogera & Webbink (1996) and is widely adopted in binary population synthesis codes for radiative MS/Hertzsprung gap (HG) donor stars.

After the mass of a star, which is the most fundamental parameter, metallicity is the next most important parameter in stellar evolution. Many observed stellar phenomena including binaries are dominated by metal-poor environments. Examples include horizontal-branch stars (Iben & Rood 1970), blue stragglers (blue metal-poor stars; Preston & Sneden 2000), Galactic halo stars (e.g., Zhao et al. 2006; Li et al. 2018), metal-poor thick disk stars (e.g., Wu et al. 2021), and the stellar initial mass function of ultrafaint dwarf satellite galaxies (Yan et al. 2020). Inspired by the important contribution to the chemical evolution of galaxies, asymptotic giant branch nucleosynthesis and supernovae physics, the abundances of carbon (Sneden 1974), nitrogen (Sneden 1973), oxygen

(Akerman et al. 2004), and supernova elements (McWilliam et al. 1995; Ryan et al. 1996) are all affected.

Zampieri & Roberts (2009) suggest that super-Eddington accretion onto stellar-mass BHs at low metallicity, rather than intermediate-mass BHs, contribute significantly to ultraluminous X-ray sources (ULXs). Belczynski et al. (2010) find that the gravitational-wave detection rate is increased by a factor of 20 if the metallicity is decreased from solar to a half and half mixture of solar and 10% solar metallicity. The chemically homogeneous evolution of stars favors a low-metallicity environment (Yoon & Langer 2005). In addition to isolated binary evolution and dynamical interaction in a dense cluster, chemically homogeneous evolution of binaries is an important source of merging BHs (de Mink & Mandel 2016; Mandel & de Mink 2016). Gravitational-wave detection discoveries are frequently merging massive stellar-mass BHs ($M > 30\ M_\odot$; Abbott et al. 2021), which have been suggested to form in metal-poor environments (e.g., Vink et al. 2021). Klencki et al. (2020) show that metallicity has a strong influence on the type of mass transfer in massive binary systems. Klencki et al. (2022) find that the metallicity of massive stars strongly influences the course and outcome of mass-transfer evolution.

Here we focus on intermediate-mass (IM) stars ($1.6 \leqslant M/M_\odot \leqslant 10$) with metallicity $Z = 0.001$. We make a comparison of the radius response of IM stars with different metallicites undergoing adiabatic mass loss. We find their critical mass ratios for dynamical timescale mass transfer. An application to IMXBs is also presented. We briefly mention methods and stellar model selection in Section 2. Using $4\ M_\odot$ stars as examples in Section 3, we study the effect of metallicity on the response of stars to adiabatic mass loss. We provide the critical mass ratios for dynamical timescale mass transfer of the IM stars in Section 4. Fitting formulae for these critical mass ratios for both $Z = 0.001$ and $Z = 0.02$ IM stars are provided in Section 5. In Sections 6 and 7, we apply our results to observed IMXBs and summarize our studies, respectively.

2. Methods and Model Selections

We use our adiabatic mass-loss model to study the responses of IM donor stars with metallicity $Z = 0.001$. The methods and numerical implementations are described in detail in Ge et al. (2010, 2015, 2020a, hereafter Papers I, II and III, respectively). We use the same physical parameters, such as mixing-length and overshooting coefficients, for metal-poor IM stars. As for Papers I–III, we build initial model sequences that undergo adiabatic mass loss without including stellar winds. The masses of the initial models are 1.6, 2.5, 4.0, 6.3, and $10.0\ M_\odot$. Radius grids are selected roughly with $\Delta \log_{10}(R/R_\odot) = 0.1$ except for the MS stars (Figure 1).

We introduce the key points of calculating the critical mass ratio, q_{ad}, for dynamical timescale mass transfer. In principle, the critical initial mass ratio is the minimum value satisfying the mass–radius exponent of the donor star, $\zeta_{\mathrm{ad}} = d\ln R/d\ln M$, which is equal to the mass–radius exponent of its Roche lobe, $\zeta_{\mathrm{L}}(q_{\mathrm{ad}}) = d\ln R_{\mathrm{L}}/d\ln M$, throughout the whole adiabatic mass-loss process. This is because the runaway mass trasfer is increased gradually as mass transfer begins. So, instead of using the surface radius of the donor star, R, we use an inner radius, R_{KH}, to calculate the mass–radius exponent, $\zeta_{\mathrm{KH}} = d\ln R_{\mathrm{KH}}/d\ln M|_{\mathrm{ad}}$. This innner radius represents the mass-loss
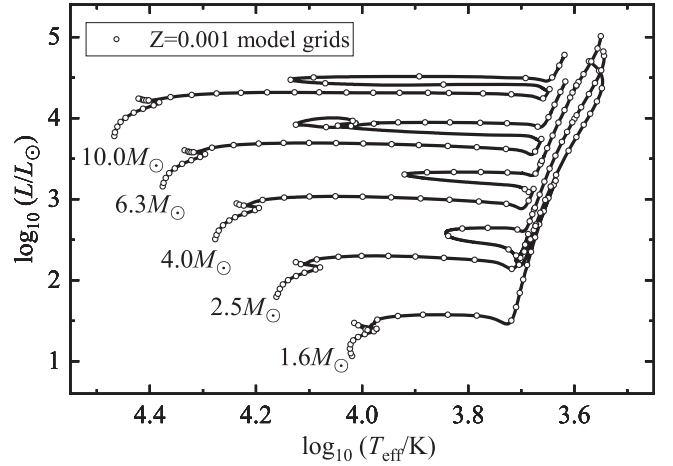

Figure 1. Hertzsprung–Russell diagram of intermediate-mass stars and model grids (circles). The masses are labeled and the metallicity is $Z = 0.001$.

rate, $\dot{M}$ (see (A9) in Paper I), reaching a thermal timescale rate $\dot{M}_{\mathrm{KH}} = M_{\mathrm{i}}/\tau_{\mathrm{KH}}$.

We count the model number n from 1 to N for the whole adiabatic mass-loss process. For the initial model $n = 1$, we have the initial mass $M_{1\mathrm{i}}$ and initial radius $R_{1\mathrm{i}}$. The Roche-lobe radius of this model is $R_{\mathrm{L,i}} = R_{1\mathrm{i}}$. The initial mass ratio $q_{\mathrm{i}} = M_{1\mathrm{i}}/M_{2\mathrm{i}}$ is unknown and to be solved. We define a mass function $\mu = M_1/(M_1 + M_2) = q/(1 + q)$ for convenience since it can only change from 0 to 1. For model number n, the mass M_n and inner radius $R_{\mathrm{KH},n}$ are solved from the adiabatic mass-loss calculation. The mass–radius exponent $\zeta_{\mathrm{ad}} = \zeta_{\mathrm{KH}}$ can be calculated from models n and $n - 1$. If we assume the mass transfer is conserved in mass and angular momentum, the mass and Roche-lobe radius exponent, ζ_{L}, is a function of the mass ratio (see Equation (45) in Paper I). Applying to the orbital angular momentum of a binary, for conserved mass transfer, we can write

$$\frac{R_{\mathrm{L}}(\mu_n)}{R_{1\mathrm{i}}} = \frac{r_{\mathrm{L}}(\mu_n)}{r_{\mathrm{L}}(\mu_{\mathrm{i}})}\left(\frac{\mu_{\mathrm{i}}}{\mu_n}\right)^2\left(\frac{1 - \mu_{\mathrm{i}}}{1 - \mu_n}\right)^2, \qquad (1)$$

where $\mu_n = \mu_{\mathrm{i}}M_n/M_{1\mathrm{i}}$, $\mu_{\mathrm{i}} = q_{\mathrm{i}}/(1 + q_{\mathrm{i}})$, and

$$r_{\mathrm{L}}(q) = \frac{0.49q^{2/3}}{0.6q^{2/3} + \ln(1 + q^{1/3})}, \qquad (2)$$

from Eggleton's approximation (Eggleton 1983). Starting from an initial guess, $\mu_{\mathrm{i}} = 0.5$, we use a bisection method to calculate the initial mass function, μ_n, satisfying both $R_{\mathrm{L},n} = R_{\mathrm{KH},n}$ and $\zeta_{\mathrm{L},n} = \zeta_{\mathrm{KH},n}$. By tracing $n = 1$ to $n = N$, we can get the minimum value of μ_{min}. So, the critical initial mass ratio is calculated finally with $q_{\mathrm{ad}} = \mu_{\mathrm{min}}/(1 - \mu_{\mathrm{min}})$.

In addition to standard donor stars with mixing-length convective envelopes, we also build parallel donor star sequences with isentropic envelopes. In these stars, convective envelopes have been replaced by isentropic ones, with the specific entropy fixed to be that at the base of envelopes. By doing this, the limitations of adiabatic approximation at the tiny layer under the photosphere are overcome. Consequently, the superadiabatic expansion in a donor star with a thick convective envelope becomes placid. We can find a more detailed explanation in Papers I, II, and III. The critical initial mass ratios $\tilde{q}_{\mathrm{ad}}$ for these donor stars can be calculated with the same method mentioned above. A $\sim$ script on the top of
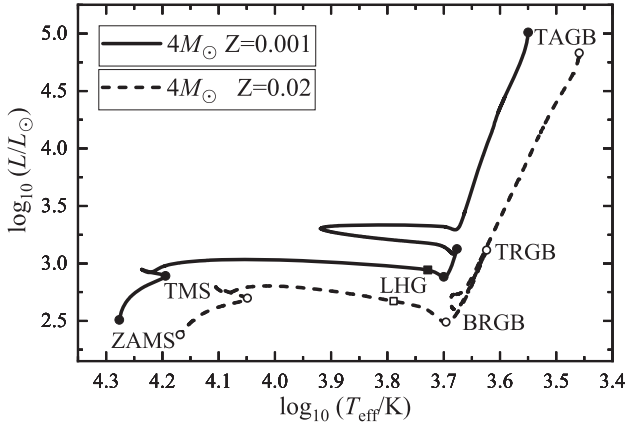
Figure 2. Theoretical Hertzsprung–Russell diagram of $4\,M_\odot$ stars with metallicities $Z = 0.001$ (solid line) and $Z = 0.02$ (dashed line). Solid and open circles show the locations of important evolutionary stages, such as the zero-age main sequence (ZAMS), the terminal-age main sequence (TMS), the base of the red giant branch (BRGB), the tip of the red giant branch (TRGB), and the tip of the asymptotic giant branch (TAGB). Filled and open squares are the late Hertzsprung–Russell gap (LHG) where the critical mass ratio reaches a maximum.

corresponding parameters, such as the inner radius $\tilde{R}_{\rm KH}$, is labeled for donor stars with replaced envelopes.

3. $4\,M_\odot$ Stars with Different Metallicities

In this section, we study the impact of metallicity on the critical mass ratio $\tilde{q}_{\rm ad}$ for dynamical timescale mass transfer of IM stars. To understand the effects of metallicity, we first consider the differences in the global physical behavior of a $M_{\rm 1i} = 4\,M_\odot$ star with metallicities of $Z = 0.001$ and $Z = 0.02$. Second, using terminal main sequence (TMS) and tip of the red giant branch (TRGB) models, we examine the response to adiabatic mass loss of $4\,M_\odot$ stars with $Z = 0.001$ and $Z = 0.02$ of different radii. Lastly, we calculate the difference in $\tilde{q}_{\rm ad}$ between solar-metallicity and metal-poor $4\,M_\odot$ donor stars. We use $Z = 0.02$ for solar metallicity despite recent studies indicating a lower metallicity in the solar atmosphere (e.g., Asplund et al. 2009).

It is well known that metal-poor MS stars are more compact, hotter, and of smaller radii (e.g., Pols 2011). Figure 2 shows that a $4\,M_\odot$ star with $Z = 0.001$ is more luminous and hotter than its $Z = 0.02$ counterpart at every evolutionary stage. The radius of a $4\,M_\odot$ metal-poor star is almost always smaller than that at solar metallicity, with the only exception near the base of the red giant branch (BRGB; see Figure 3). This leads to a slightly larger HG for the metal-poor star. However, it has a larger core mass (see Figure 4). This leads to a smaller evolutionary range on the red giant branch (RGB).

The radiative envelope dominates its radius response to the adiabatic mass loss for IM stars on the MS or in the HG. Therefore, an initial shrinkage of the radius is expected during the mass loss. However, after the IM star evolves to the RGB or the asymptotic giant branch (AGB), the rapidly growing convective envelope dominates the radius response to adiabatic mass loss. Therefore, an initial radius expansion is followed for a RGB/AGB star during mass loss. Because the responses of donor stars with radiative and convective envelopes are different, we choose two stellar models at the TMS and TRGB as examples. In the following, we first show the critical mass
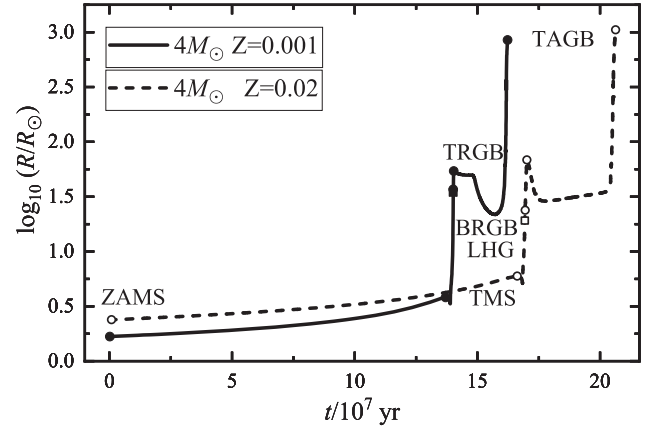

Figure 3. Radii R of $4\,M_\odot$ stars with metallicities $Z = 0.001$ (solid line) and $Z = 0.02$ (dashed line) as a function of age t. Lines and symbols correspond with those of Figure 2.
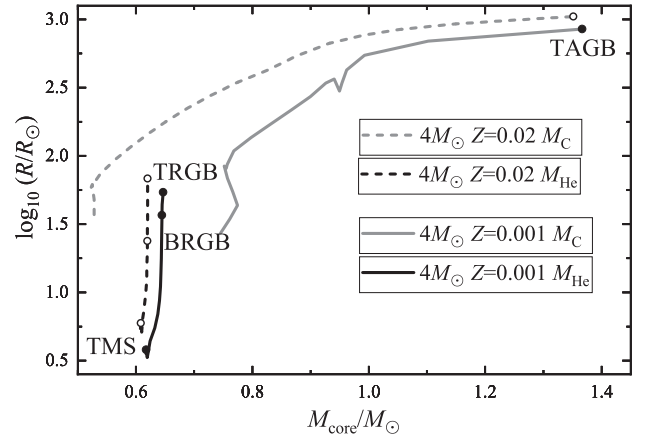

Figure 4. Radii R of $4\,M_\odot$ stars with metallicities $Z = 0.001$ (solid lines) and $Z = 0.02$ (dashed lines) as a function of their core masses. The helium core mass ($M_{\rm He}$, black lines) is where the maximum mass fraction of hydrogen is 0.15, and the carbon core mass ($M_{\rm C}$, gray lines) is where the maximum mass fraction of helium is 0.25. Solid and open circles correspond with those in Figure 2. Note that the helium core only appears after the hydrogen is exhausted in the convective core.

ratios of two example models with $Z = 0.001$. Then, we demonstrate the impact of metallicity on the critical mass ratio.

We apply the calculation method described in the previous section to metal-poor $3.56\,R_\odot$ TMS and $54.09\,R_\odot$ TRGB models (Figure 5). The left panel of Figure 5 shows the TMS donor's critical initial mass ratio $\tilde{q}_{\rm ad} = 2.934$. If the initial mass ratio $q_{\rm i} < \tilde{q}_{\rm ad}$ the mass transfer is dynamically stable and vice versa. The curves of the radius of the TMS donor star and its Roche-lobe radius show delayed dynamical instability. Its Roche-lobe radius curve is tangent with the donor's inner radius at $\tilde{M}_{\rm KH} = 2.636\,M_\odot$. For this radiative envelope star, the inner radius $\tilde{R}_{\rm KH}$ and its isentropic envelope radius are almost identical to its radius during the adiabatic mass loss. The right panel of Figure 5 presents the TRGB donor's critical initial mass ratio $\tilde{q}_{\rm ad} = 1.265$. The inner radius of this TRGB donor is tangent with its Roche-lobe radius at $\tilde{M}_{\rm KH} = 3.328\,M_\odot$. This TRGB donor's extended and low-density convective envelope makes the inner radius $\tilde{R}_{\rm KH}$ much smaller than its radius, but not the same after the core is exposed. We expect binary systems with
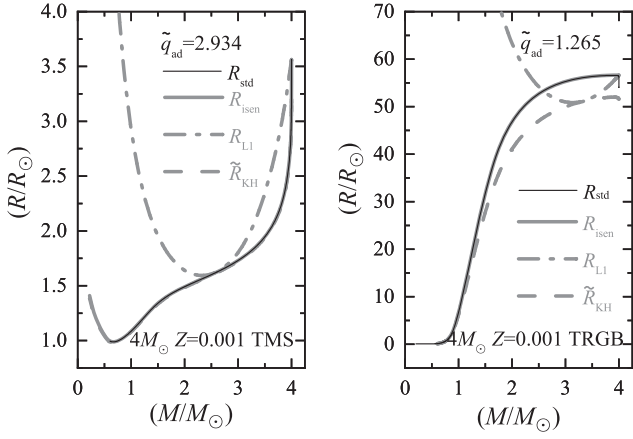
Figure 5. Radial response curves for a 4 $M_\odot$ ($Z = 0.001$) TMS star (left panel) and a TRGB star. Solid lines trace the adiabatic mass-loss sequences. Thin black solid lines represent standard stars; thick gray solid lines represent correspondingly isentropic envelope stars. Gray dashed lines are shown for the inner radii $\tilde{R}_{KH}$ where the mass-loss rate reaches $\dot{M}_{KH}$. Gray dashed–dotted lines mark the Roche-lobe radius as a function of mass for critical initial mass ratios $\tilde{q}_{ad}$. The corresponding limits for standard models such as R_{KH} and q_{ad} are omitted for clarity.

this TRGB donor will evolve to the common-envelope phase if the initial mass ratio is more significant than 1.265.

The differences in the entropy profiles between the two TMS stars with $Z = 0.001$ and $Z = 0.02$ are negligible. As such, the radius responses have the same trend (Figure 6). However, the $Z = 0.001$ TMS star has a larger convective core (Figure 4) and a smaller radiative envelope. This diminishes the contraction of the metal-poor star (see the right panel of Figure 6). Consequently, the critical mass ratio for dynamical timescale mass transfer of the metal-poor star at each evolutionary stage is smaller (Figure 7). The critical mass ratios of donor stars with different metallicities have the same trend. $\tilde{q}_{ad}$ depends on its evolutionary stage for a given mass star. From the zero-age main sequence (ZAMS) to the late Hertzsprung–Russell gap (LHG; where $\tilde{q}_{ad}$ reaches a maximum) $\tilde{q}_{ad}$ increases almost linearly with the logarithm of the stellar radius. Then, a sudden drop of $\tilde{q}_{ad}$ indicates the switching from a radiative-dominated structure to a convective-dominated one. From slightly late BRGB to TAGB (neglecting core-helium burning stages), $\tilde{q}_{ad}$ increases again with the radius.

At the TRGB the radius response is dominated by the deep convective envelope. However, the partial ionization and nonideal gas effects change the behavior from that of simplified polytropic models. In fact, the critical mass ratios for dynamical timescale mass transfer differ greatly between realistic stars and those with a polytropic equation of state (see Figure 9 in Paper III). The response of the thin layer under the photospheric surface might be dominated by radiation. The initial superadiabatic expansion in the right panel of Figure 8 might be overestimated by the adiabatic assumption, so we build isentropic envelope models to offset part of the superadiabatic expansion (see details in Papers I–III). The metal-poor model has a larger helium core than the solar-metallicity model. As such, the convective envelope of the metal-poor star is thinner. Also, the thermal timescales of metal-poor RGB/AGB stars are systematically shorter than those of solar-metallicity stars at the same radius. So, the critical mass ratios of metal-poor stars are larger than solar-metallicity stars with the same radii.
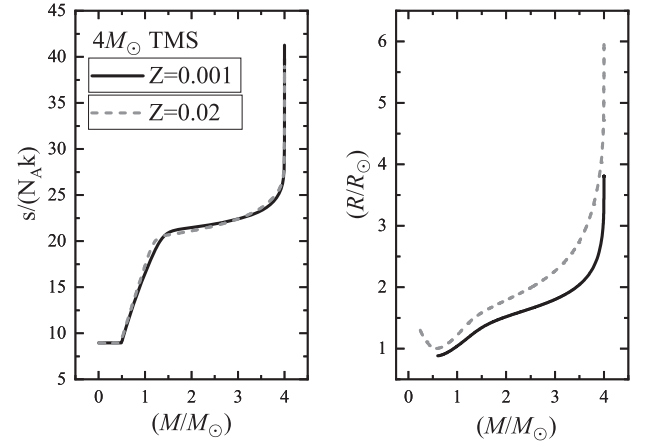

Figure 6. Specific entropy s profile (left panel) and the remnant radius R as a function of mass M (right panel). Solid and dashed lines represent 4 $M_\odot$ TMS stars with $Z = 0.001$ and $Z = 0.02$, respectively. We used gray dashed lines to make the overlap region distinguishable.
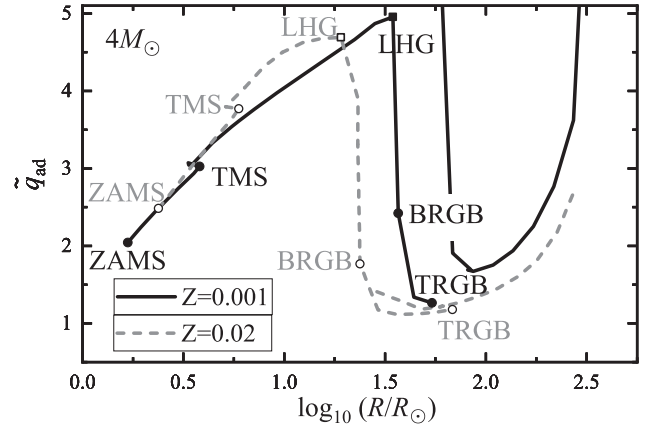
Figure 7. Critical mass ratios $\tilde{q}_{ad}$ as a function of the donor's initial radius R. Lines and symbols have the same meaning as in Figures 2 and 3.

Figure 8. As Figure 6 but for 4 $M_\odot$ TRGB stars.

In summary, for a metal-poor MS and HG donor star, we find $\tilde{q}_{ad}$ is smaller than for a solar-metallicity star at the same evolutionary stage. For a metal-poor RGB/AGB donor star we find $\tilde{q}_{ad}$ is larger than for a solar-metallicity star at the same radius.

Table 1
Properties and Critical Mass Ratios of Initial Stellar Models

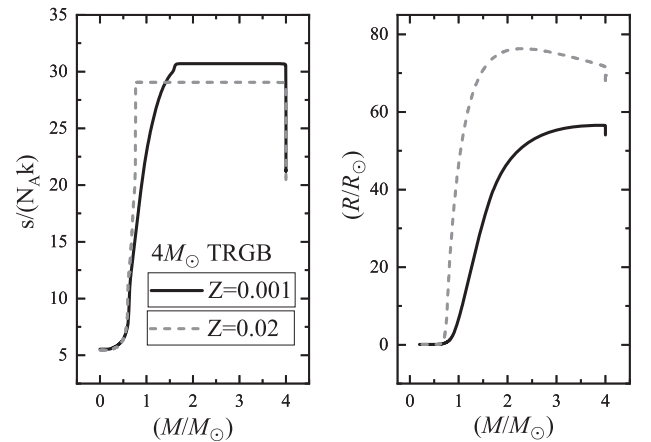| k ⋯	$\log_{10} t$ /yr	M /$M_\odot$	$\log_{10} R$ /$R_\odot$	M_{ce} /$M_\odot$	M_{He} /$M_\odot$	M_C /$M_\odot$	$\log_{10} T_e$ /K	$\log_{10} L$ /$L_\odot$	X_s ⋯	ρ_c /g cm^{-3}	T_c /K	q_{ad} ⋯	M_{KH} /$M_\odot$	$\tilde{q}_{ad}$ ⋯	$\tilde{M}_{KH}$ /$M_\odot$
1	⋯	4.0	0.224	0.000	0.000	0.000	4.277	2.508	0.756	1.613	7.462	2.042	2.478	2.044	2.477
2	7.4528	4.0	0.254	0.000	0.000	0.000	4.274	2.558	0.756	1.605	7.469	2.132	2.498	2.134	2.501
3	7.7343	4.0	0.289	0.000	0.000	0.000	4.270	2.612	0.756	1.603	7.478	2.237	2.525	2.238	2.525
4	7.9073	4.0	0.338	0.000	0.000	0.000	4.262	2.677	0.756	1.606	7.491	2.378	2.554	2.380	2.554
5	8.0020	4.0	0.391	0.000	0.000	0.000	4.250	2.736	0.756	1.616	7.505	2.523	2.581	2.525	2.580
6	8.0485	4.0	0.433	0.000	0.000	0.000	4.239	2.775	0.756	1.630	7.516	2.633	2.599	2.635	2.597
7	8.0915	4.0	0.491	0.000	0.000	0.000	4.222	2.822	0.756	1.660	7.533	2.781	2.620	2.783	2.618
8	8.1212	4.0	0.552	0.000	0.617	0.000	4.202	2.863	0.756	1.717	7.557	2.932	2.636	2.934	2.636
9	8.1361	4.0	0.580	0.000	0.618	0.000	4.194	2.891	0.756	1.810	7.589	3.024	2.649	3.026	2.648
10	8.1420	4.0	0.524	0.000	0.619	0.000	4.236	2.946	0.756	2.293	7.688	3.071	2.673	3.074	2.672
11	8.1421	4.0	0.527	0.000	0.620	0.000	4.231	2.931	0.756	2.427	7.662	3.041	2.668	3.044	2.667
12	8.1422	4.0	0.538	0.000	0.620	0.000	4.223	2.921	0.756	2.519	7.648	3.034	2.670	3.038	2.669
13	8.1427	4.0	0.643	0.000	0.624	0.000	4.187	2.989	0.756	2.879	7.632	3.325	2.693	3.327	2.693
14	8.1437	4.0	0.739	0.000	0.632	0.000	4.147	3.018	0.756	3.224	7.670	3.536	2.706	3.539	2.705
15	8.1445	4.0	0.841	0.000	0.638	0.000	4.099	3.031	0.756	3.488	7.739	3.739	2.717	3.742	2.716
16	8.1449	4.0	0.940	0.000	0.640	0.000	4.050	3.034	0.756	3.667	7.798	3.929	2.730	3.932	2.729
17	8.1453	4.0	1.041	0.000	0.642	0.000	3.999	3.031	0.756	3.797	7.844	4.114	2.747	4.119	2.746
18	8.1455	4.0	1.144	0.000	0.643	0.000	3.945	3.022	0.756	3.894	7.880	4.292	2.767	4.301	2.766
19	8.1456	4.0	1.248	0.000	0.644	0.000	3.890	3.008	0.756	3.967	7.908	4.455	2.785	4.482	2.781
20	8.1458	4.0	1.349	0.000	0.644	0.000	3.835	2.991	0.756	4.021	7.928	4.603	2.788	4.665	2.780
21	8.1458	4.0	1.449	0.000	0.644	0.000	3.780	2.970	0.756	4.062	7.944	4.752	2.772	4.871	2.759
22	8.1459	4.0	1.538	0.000	0.645	0.000	3.728	2.942	0.756	4.096	7.957	4.747	2.770	4.956	2.747
23	8.1460	4.0	1.565	0.249	0.645	0.000	3.700	2.883	0.756	4.154	7.979	2.082	3.763	2.421	3.763
24	8.1462	4.0	1.643	1.318	0.645	0.000	3.686	2.982	0.756	4.211	8.001	1.173	3.609	1.339	3.448
25	8.1467	4.0	1.733	2.305	0.647	0.000	3.677	3.125	0.753	4.206	8.096	1.091	3.522	1.265	3.328
26	8.1632	4.0	1.696	0.647	0.859	0.000	3.686	3.089	0.753	3.878	8.126	1.613	3.682	1.884	3.564
27	8.1680	4.0	1.698	0.139	0.902	0.000	3.693	3.124	0.753	3.839	8.134	3.688	3.871	4.503	3.273
28	8.1961	4.0	1.336	0.000	1.149	0.000	3.920	3.303	0.753	3.693	8.200	5.975	2.904	6.000	2.902
29	8.2039	4.0	1.434	0.000	1.203	0.745	3.877	3.330	0.753	3.752	8.248	6.463	2.934	6.528	2.929
30	8.2056	4.0	1.537	0.000	1.214	0.761	3.827	3.334	0.753	3.805	8.271	6.854	2.945	6.992	2.937
31	8.2064	4.0	1.638	0.000	1.219	0.774	3.776	3.333	0.753	3.849	8.288	7.254	2.941	7.518	2.928
32	8.2068	4.0	1.736	0.000	1.221	0.766	3.726	3.329	0.753	3.885	8.300	7.613	2.930	8.147	2.908
33	8.2074	4.0	1.835	1.050	1.225	0.757	3.673	3.315	0.753	4.183	8.385	1.582	3.588	1.906	3.435
34	8.2075	4.0	1.925	1.922	1.225	0.752	3.662	3.452	0.753	4.509	8.431	1.378	3.468	1.693	3.265
35	8.2076	4.0	1.910	1.824	1.225	0.755	3.664	3.428	0.753	4.600	8.435	1.381	3.484	1.691	3.284
36	8.2076	4.0	1.937	2.055	1.224	0.757	3.661	3.471	0.753	4.758	8.457	1.357	3.453	1.673	3.243
37	8.2078	4.0	2.036	2.469	1.223	0.768	3.651	3.629	0.751	5.130	8.504	1.375	3.369	1.754	3.132
38	8.2080	4.0	2.134	2.641	1.222	0.798	3.641	3.784	0.747	5.403	8.536	1.459	3.281	1.937	3.029
39	8.2081	4.0	2.235	2.718	1.221	0.833	3.630	3.943	0.744	5.740	8.572	1.611	3.189	2.251	2.925
40	8.2082	4.0	2.337	2.762	1.219	0.867	3.618	4.100	0.741	6.135	8.582	1.846	3.094	2.766	2.828
41	8.2083	4.0	2.435	2.945	1.058	0.900	3.608	4.253	0.700	6.572	8.487	2.197	2.989	3.621	2.720
42	8.2084	4.0	2.532	3.039	0.961	0.926	3.596	4.401	0.676	6.895	8.338	4.041	2.893	8.702	2.589
43	8.2084	4.0	2.562	3.046	0.954	0.940	3.592	4.445	0.675	7.025	8.280	5.678	2.835	10.594	2.531
44	8.2084	4.0	2.474	3.046	0.953	0.950	3.603	4.315	0.675	7.111	8.244	2.524	2.973	5.053	2.701
45	8.2084	4.0	2.533	3.044	0.956	0.954	3.596	4.402	0.675	7.209	8.192	4.054	3.006	⋯	⋯
46	8.2085	4.0	2.630	3.037	0.963	0.962	3.583	4.543	0.675	7.300	8.134	⋯	⋯	⋯	⋯
47	8.2086	4.0	2.738	3.007	0.993	0.992	3.568	4.700	0.673	7.436	8.071	⋯	⋯	⋯	⋯
48	8.2091	4.0	2.841	2.898	1.102	1.102	3.556	4.858	0.667	7.780	8.090	⋯	⋯	⋯	⋯
49	8.2098	4.0	2.929	2.633	1.367	1.367	3.550	5.010	0.665	9.278	8.439	⋯	⋯	⋯	⋯

Note. M_{KH} is the mass at which the stellar inner radius R_{KH} is equal to its Roche-lobe radius R_L for the critical mass ratio q_{ad}. $\tilde{M}_{KH}$ has the same meaning as M_{KH} but for isentropic envelope stars; see Figures 4 and 6 in Paper I for more detail. The value of $M_{1i} - M_{KH}$ or $M_{1i} - \tilde{M}_{KH}$ indicate whether a prompt or a delayed dynamical instability occurs. This table is available in its entirety in machine-readable form.

(This table is available in its entirety in machine-readable form.)

4. Results

Table 1 summarizes both the initial global and interior physical parameters of our $Z = 0.001$ IM stars. Typically, the lower- and upper-mass limits for an IM star with solar metallicity are around 2.1 $M_\odot$ and 8 $M_\odot$. We select here from 1.6 $M_\odot$ and 10.0 $M_\odot$ to cover the metallicity effects and a broader range of mass.

The key parameters are as follows: k is a mass-loss sequence number, t is the age, M is the mass of the initial model, R is the initial radius, M_{ce} is the mass of the convective envelope, M_{He} is the mass of the helium core, where the mass fraction of X_H is 0.15, M_C is the mass of the carbon core, where the mass fraction of X_{He} is 0.25, T_e is the effective temperature, L is the stellar luminosity, X_s is the surface hydrogen abundance
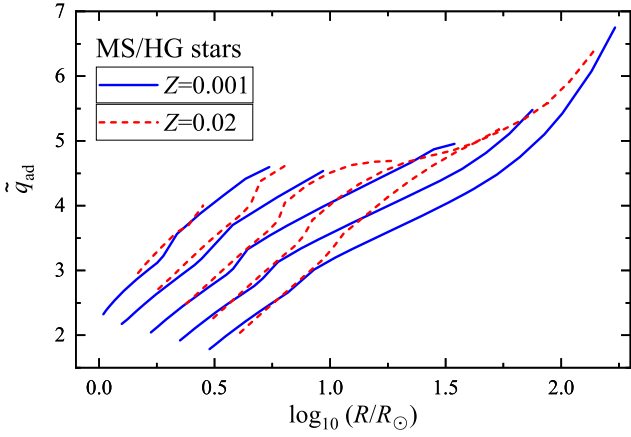
Figure 9. Critical mass ratios as a function of the radii of MS/HG donor stars. Blue solid and red dashed lines are metal-poor and solar-metallicity stars, respectively. From left to right, the masses of the different lines are 1.6 $M_\odot$, 2.5 $M_\odot$, 4.0 $M_\odot$, 6.3 $M_\odot$, and 10.0 $M_\odot$. For clarity, plots end at the maximum of $\tilde{q}_{ad}$ in the late HG.

Figure 10. Similar to Figure 9 but for RGB/AGB stars. For clarity, plots start from the minimum of $\tilde{q}_{ad}$ on the early RGB.

(fraction by mass), ρ_c is the central density, T_c is the central temperature, q_{ad} is the critical mass ratio for dynamical timescale mass transfer, M_{KH} is the mass threshold at which $\dot{M} = -M/\tau_{KH}$, $\tilde{q}_{ad}$ is the critical mass ratio for dynamical timescale mass transfer in the case of an isentropic envelope, and $\tilde{M}_{KH}$ is the mass threshold at which $\dot{M} = -M/\tau_{KH}$ in that case. The second row in Table 1 lists accordingly the units of these physical variables.

The critical mass ratios $\tilde{q}_{ad}$ listed in the extended version of Table 1 are also partially represented in graphical form in Figures 9 and 10. We see that $\tilde{q}_{ad}$ decreases almost linearly with the logarithm of radius at the BRGB region from the late HG to the early RGB. As we found in the last section, $\tilde{q}_{ad}$ is smaller for MS/HG metal-poor stars at the same evolutionary stage. Conversely, $\tilde{q}_{ad}$ is larger for RGB/AGB metal-poor stars. We provide both tabular and graphical forms for our results in this section. We find the fitting formulae for the critical mass ratios as functions of masses and radii in the next section.

5. Fitting Formulae

The instability criteria for dynamical timescale mass transfer provide us with onset thresholds for common-envelope evolution. This is one of the key physical inputs for binary population synthesis. Interpolation in the tables provide accurate criteria at the cost of calculating speed. Alternatively, we find fitting formulae for both $Z = 0.001$ and $Z = 0.02$ (Paper III) IM stars with masses from 1.6 $M_\odot$ to 10.0 $M_\odot$.

For MS donor stars, there is a linear relationship between the critical mass ratio and the logarithm of mass and radius (see also Ge et al. 2013):

$$\tilde{q}_{ad} = a + b \times \log_{10}\left(\frac{M}{M_\odot}\right) + c \times \log_{10}\left(\frac{R}{R_\odot}\right). \quad (3)$$

The coefficients a, b, and c for metal-poor and solar-metallicity IM stars are given in Table 2 and Figures 11 and 12. We find that the fitting formulas for MS donor stars are simply and accurately fitted. The maximum and average absolute fractional deviation are 4.94% and 1.01% for $Z = 0.001$ MS stars. The corresponding values are 2.09% and 0.42% for $Z = 0.02$ MS stars.
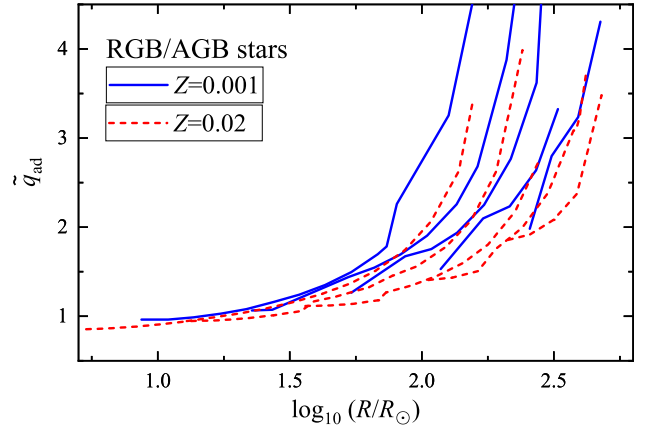
The mass fraction of the radiative envelope of the MS/HG donor star increases monotonically from the ZAMS to the late HG. However, the gradient of $\tilde{q}_{ad}$ as a function of $\log_{10} R$ differs for HG and MS donor stars (Figure 9). As such, we use a fitting formula for MS/HG stars as follows:

$$\tilde{q}_{ad} = q_{min} + \frac{a \times [(R - R_{min})/R_\odot]^{1/2} + b \times [(R - R_{min})/R_\odot]^{1/4}}{1 + c \times [(R - R_{min})/R_\odot]^{7/8}}, \quad (4)$$

where q_{min} and R_{min} are the critical mass ratio and radius of the ZAMS models, respectively. The coefficients a, b, and c for MS/HG stars are given in Table 2. Equation (4) is valid for donor stars with radii R from R_{min} to R_{max}. R_{max} is the radius of a donor star at the LHG where the critical mass ratio reaches a maximum. For $Z = 0.001$ IM stars, we have

$$q_{min} = q_{ZAMS} = 2.45122 - 0.66844 \times \log_{10}\left(\frac{M}{M_\odot}\right), \quad (5)$$

$$\frac{R_{min}}{R_\odot} = \frac{R_{ZAMS}}{R_\odot} = -0.2922 + \left(\frac{M}{M_\odot}\right)^{0.51}, \quad (6)$$

and

$$\log_{10}\left(\frac{R_{max}}{R_\odot}\right) = 0.29534 + 1.95688 \times \log_{10}\left(\frac{M}{M_\odot}\right). \quad (7)$$

For $Z = 0.02$ IM stars, we have

$$q_{min} = q_{ZAMS} = 3.18500 - 1.15243 \times \log_{10}\left(\frac{M}{M_\odot}\right), \quad (8)$$

$$\frac{R_{min}}{R_\odot} = \frac{R_{ZAMS}}{R_\odot} = -0.09996 + \left(\frac{M}{M_\odot}\right)^{0.60}, \quad (9)$$

and

$$\log_{10}\left(\frac{R_{max}}{R_\odot}\right) = -0.01035 + 2.15399 \times \log_{10}\left(\frac{M}{M_\odot}\right). \quad (10)$$

Figures 13 and 14 show the fitted criteria as functions of the initial mass and radius of MS/HG stars. The fits are not as good as for the MS but still provide the basic trends. For $Z = 0.001$ MS/HG stars the max and average absolute

Table 2
Fitting Formulae and Coefficients

Stage	Z	Formula	a	b	c	q_{min}	R_{min}	R_{max}
MS	0.001	Equation (3)	2.88940	−2.46266	2.80378	⋯	⋯	⋯
MS	0.02	Equation (3)	3.09721	−3.05344	3.24722	⋯	⋯	⋯
MS/HG	0.001	Equation (4)	3.72324 $-0.79775 \times (M/M_\odot)$ $+0.04619 \times (M/M_\odot)^2$	−2.26829 $+0.56558 \times (M/M_\odot)$ $-0.03254 \times (M/M_\odot)^2$	0.19792 $-0.04750 \times (M/M_\odot)$ $+0.00278 \times (M/M_\odot)^2$	Equation (5)	Equation (6)	Equation (7)
MS/HG	0.02	Equation (4)	0.75208 $+0.39155 \times (M/M_\odot)$ $-0.03915 \times (M/M_\odot)^2$	0.13486 $-0.50319 \times (M/M_\odot)$ $+0.04552 \times (M/M_\odot)M^2$	−0.36874 $+0.23056 \times (M/M_\odot)$ $-0.03658 \times (M/M_\odot)^2$ $+0.001732 \times (M/M_\odot)^3$	Equation (8)	Equation (9)	Equation (10)
RGB/AGB	0.001	Equation (11)	0.01066 $-9.82603\text{E-}4 \times (M/M_\odot)$ $-2.95245\text{E-}4 \times (M/M_\odot)^2$	−1.18954E-6 $+5.61586\text{ E-}6 \times (M/M_\odot)$ $+6.02668\text{ E-}7 *(M/M_\odot)^2$	−0.005901 $+0.001507 \times (M/M_\odot)$	Equation (12)	Equation (13)	⋯
RGB/AGB	0.02	Equation (11)	0.01595 $-0.00526 \times (M/M_\odot)$ $+3.64794\text{ E-}4 \times (M/M_\odot)^2$	−8.39047E-5 $+4.21662\text{ E-}5 \times (M/M_\odot)$ $-5.14285\text{E-}6 \times (M/M_\odot)^2$ $+1.77890\text{E-}7 \times (M/M_\odot)^3$	−0.00897 $+0.00291 \times (M/M_\odot)$ $-2.19604\text{E-}4 \times (M/M_\odot)^2$	Equation (14)	Equation (15)	⋯

Note. "Min" is the abbreviation of minimum, "max" for maximum, and "avg" for average.
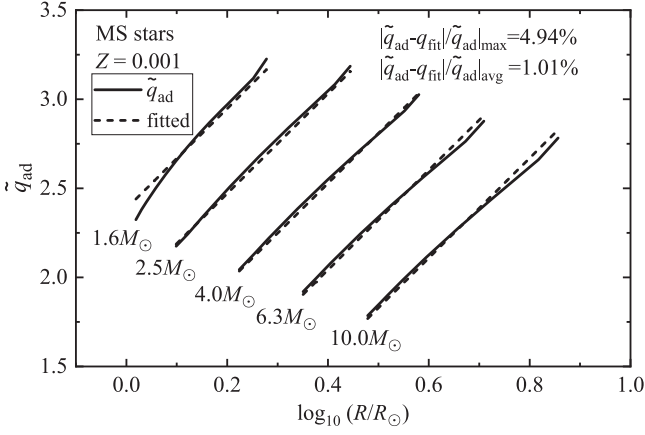
Figure 11. Critical mass ratios $\tilde{q}_{ad}$ (solid lines) and the fitted results (dashed lines), functions of the mass and radius for $Z = 0.001$ MS stars. These are linearly correlated with the logarithm of mass and radius of the star.
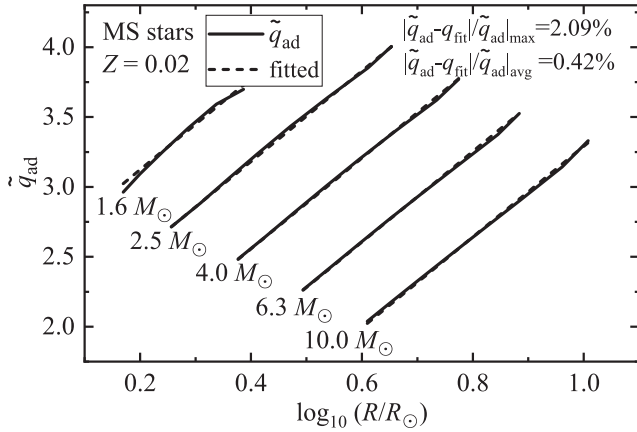

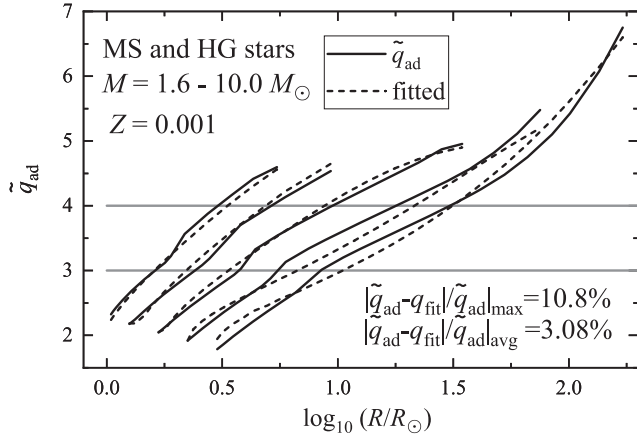**Figure 12.** Similar to Figure 11 but for $Z = 0.02$ MS stars.

Figure 13. Critical mass ratios (solid lines) and the fitted results (dashed lines) as functions of radius for $Z = 0.001$ MS/HG stars. From left to right, masses are $1.6\,M_\odot$, $2.5\,M_\odot$, $4.0\,M_\odot$, $6.3\,M_\odot$, and $10.0\,M_\odot$. The fitting formulae, coefficients, and the radius ranges are given in Table 2.

fractional deviation are 10.8% and 3.08%, respectively. The corresponding values for $Z = 0.02$ MS/HG stars are 5.32% and 2.03%.

For RGB/AGB IM stars,

$$\tilde{q}_{ad} = q_{min} + \frac{a \times (R/R_\odot) + b \times (R/R_\odot)^2}{1 + c \times (R/R_\odot)}, \qquad (11)$$
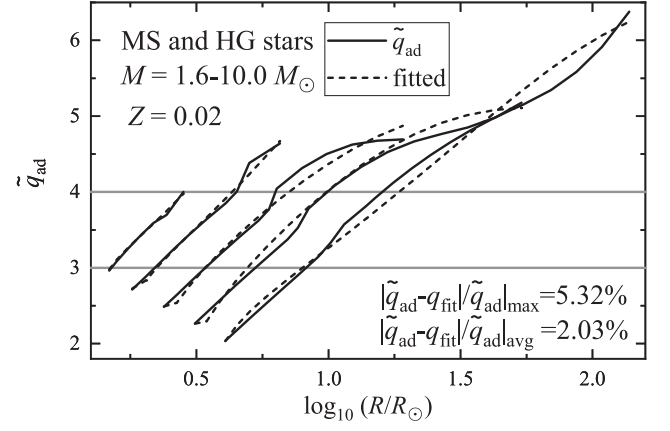

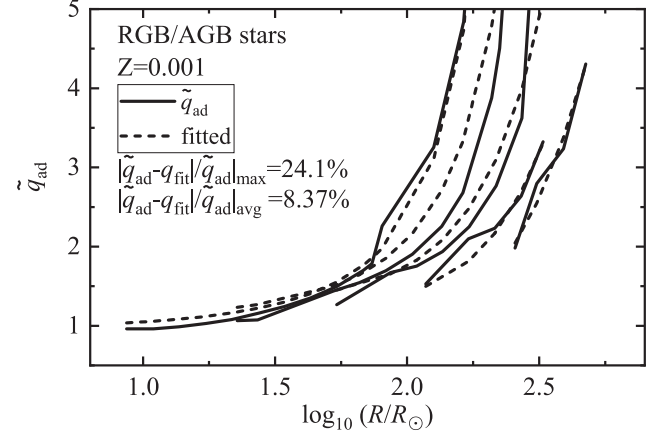**Figure 14.** Similar to Figure 13 but for $Z = 0.02$ MS/HG stars.

Figure 15. Similar to Figure 13 but for $Z = 0.001$ RGB/AGB stars. For late AGB stars, we suggest setting an upper limit around 2–3 for $\tilde{q}_{ad}$. This is because the critical mass ratio for outer Lagrangian point overflow on a thermal timescale becomes more important (see Figure 9 by Ge et al. 2020b).

where q_{min} is the minimum critical mass ratio near but slightly after the BRGB.

The coefficients a, b, and c for metal-poor and solar-metallicity RGB/AGB stars are given in Table 2. Equation (11) is suitable for donor stars with radii R from R_{min}^{GB} to R_{TRGB}. For $Z = 0.001$ IM stars, we have

$$q_{min} = 0.76856 + 0.12128 \times \left(\frac{M}{M_\odot}\right), \qquad (12)$$

$$\log_{10}\left(\frac{R_{min}^{GB}}{R_\odot}\right) = 0.59991 + 1.83362 \times \log_{10}\left(\frac{M}{M_\odot}\right). \qquad (13)$$

For $Z = 0.02$ IM stars, we have

$$q_{min} = 0.64877 + 0.12029 \times \left(\frac{M}{M_\odot}\right), \qquad (14)$$

$$\log_{10}\left(\frac{R_{min}^{GB}}{R_\odot}\right) = 0.31947 + 2.05377 \times \log_{10}\left(\frac{M}{M_\odot}\right). \qquad (15)$$

Figures 15 and 16 show the fitted criteria as a function of the initial mass and radius of RGB/AGB stars. The critical mass ratio $\tilde{q}_{ad}$ increases gradually from less than 1 to larger than 3. This is due to the competition between an increasing
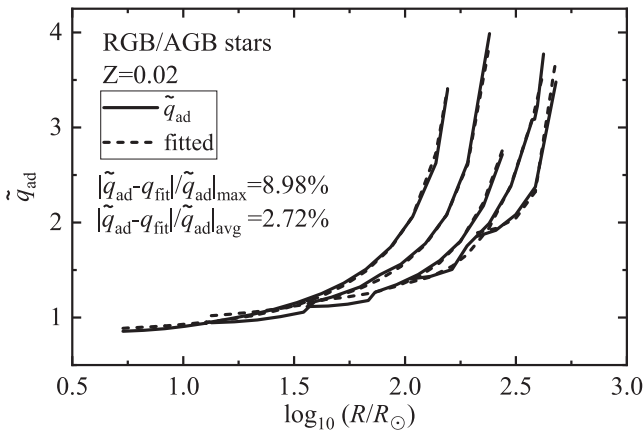
Figure 16. Similar to Figure 15 but for $Z = 0.02$ RGB/AGB stars.

convective envelope and the decreasing thermal timescale. We take $k = 37$ and $k = 38$ of $4\,M_\odot$ $Z = 0.001$ AGB donor stars as two examples. The convective envelope mass increases from 2.47 to $2.64\,M_\odot$. We expect the critical mass ratio to decrease as the convective envelope grows, as according to Hjellming & Webbink ([1987](#)). However, the Kelvin–Helmholtz timescale decreases from 1082 to 604 yr. Consequently, $\dot{M}_{KH}$ decreases from 3.13 to $3.03\,M_\odot$ and $\tilde{R}_{KH}/\tilde{R}_i$ decreases from 0.76 to 0.70 at the tangent point (similar with the right panel of Figure [5](#)). So the critical mass ratio $\tilde{q}_{ad}$ increases instead from 1.75 to 1.94. The fitting formula's maximum and average absolute fractional deviation are 8.98% and 2.72% for $Z = 0.02$ RGB/AGB stars. The accuracy of the fitting formula for $Z = 0.001$ RGB/AGB stars is not as good as for solar-metallicity stars. The maximum deviation is 24.1% for $2.5\,M_\odot$ stars. However, the average deviation of all RGB/AGB stars is acceptable (8.37%).

It is important that $\tilde{q}_{ad}$ drops dramatically around the base of the RGB, from the very late HG to the very early RGB (Figure [7](#)). This change is caused by the switch from a radiatively dominated to a convectively dominated envelope of the donor star. Thus, from R_{max} of HG to R_{min}^{GB}, $\tilde{q}_{ad}$ can be linearly interpolated by the logarithm of the radius.

6. Discussions

It is generally believed that bright Galactic X-ray sources are powered by accreting NSs or BHs in binary systems (e.g., Tauris & van den Heuvel [2006](#)). Among X-ray binary systems, over 90% are high-mass X-ray binaries (HMXBs; donor mass $M_d \geqslant 10\ M_\odot$) undergoing wind or atmosphere Roche-lobe overflow (RLOF) and LMXBs (donor mass $M_d \leqslant 1\ M_\odot$) suffering RLOF (Tauris & van den Heuvel [2006](#)). The donor in an IMXB transfers mass to the compact accretor in a thermal/subthermal timescale, and the mass transfer is dynamically stable but nonconserved (e.g., Podsiadlowski & Rappaport [2000](#); Tauris et al. [2000](#); Podsiadlowski et al. [2002](#); Shao & Li [2012](#), etc). Since IMXBs are binary systems that avoid the common-envelope process, we use them to compare their mass ratios with critical values for dynamical timescale mass transfer.

We explore catalogs of LMXBs (Ritter & Kolb [2003](#); Liu et al. [2007](#)), HMXBs (Liu et al. [2006](#)), and a paper regarding ULXs (e.g., Misra et al. [2020](#)). A cross-check is made with the more extensive catalogs BlackCAT (Corral-Santana et al. [2016](#)),

WATCHDOG (Tetarenko et al. [2016](#)), and a catalog of ULXs (Walton et al. [2022](#)). We pick out 17 IMXBs and candidates with known orbital periods and mass ratios (Table [3](#)). In the following subsections, we first check our theoretical prediction of the critical mass ratios and the observed mass ratios of IMXBs as a function of orbital periods. We then predict the upper and lower X-ray luminosities, L_X, of IMXBs and make a comparison with observed IMXBs.

6.1. Mass Ratios of Intermediate-mass X-Ray Binaries

We assume all IMXBs are undergoing RLOF. This assumption should be valid for most objects, although some might only fill around 90% of their Roche lobes. We plot the critical mass ratios $\tilde{q}_{ad}$ of IM stars on the ZAMS, TMS, and LHG ($\tilde{q}_{ad}^{max}$) as a function of orbital period, P_{orb}, as solid ($Z = 0.001$) and dashed ($Z = 0.02$) lines in Figures [17](#) and [18](#). If $q \geqslant \tilde{q}_{ad}$ when the donor first fills its Roche lobe, delayed dynamical timescale mass transfer and common-envelope evolution would have altered the system. Thus, IMXBs should all have $q < \tilde{q}_{ad}$ now to have survived. The mass ratios $q \equiv M_d/M_X$ of observed IMXBs are nicely located under the critical mass ratio limit, except for those with an eccentric orbit. We find our prediction is consistent with both shorter and longer orbital period IMXBs. Compared with the constant critical mass ratios $q = 4$ for HG stars, our parameters space (P_{orb} and q) to form longer-period ($P_{orb} > 1$ days) IMXBs is slightly larger. On the contrary, our parameters space to form shorter-period ($P_{orb} < 3$ days) IMXBs with MS donors is marginally smaller.

We need to keep in mind that mass ratio determination is less accurate than that of the orbital period. The absolute masses of the donor star and the compact accretor are less accurate than the mass ratios. Hence, multiple mass ratio estimates exist for the same object. The NS mass might be too low for SS 433 (D'Odorico et al. [1991](#)) and Her X-1 (Nagase [1989](#)), but the mass ratio should be meaningful. The accretor in SS 433 is not definitely known, but is broadly accepted to be a BH. SS 433 is one of the youngest X-ray binaries (Li [2020](#), and references therein). This tends to explain why the mass ratio of SS 433 is larger than most of the observed IMXBs with a BH companion. Only the lower limits for the mass ratios of 2S 1417–624 (Finger et al. [1996](#)) and M82 X-2 (Bachetti et al. [2014](#)) are available. In addition to the minimum value, the donor mass of KS 1947+300 (Galloway et al. [2004](#)) could be at least up to $10\,M_\odot$, implying an inclination of 38°. The most probable donor mass (for an inclination of 60°) of 4U 1901+03 (Galloway et al. [2005](#)) is $6\,M_\odot$. Galloway et al. ([2005](#)) mention the NS in 4U 1901+03 probably accretes from the wind of an MS OB star. However, the X-ray luminosity, $L_X = 1.1 \times 10^{38}$ erg s^{-1}, is high enough, and the donor star could overfill its Roche lobe at the HG. As such, we keep this source in Figure [17](#). The X-ray luminosity of HD 49798's IMXB is quite low, at $\sim 1.0 \times 10^{32}$ erg s^{-1}. The hot subdwarf donor of HD 49798 might be undergoing wind mass transfer at a rate of $2.1 \times 10^{-9}\,M_\odot$ yr^{-1} (Mereghetti et al. [2021](#)). As such, we mark this object as gray in Figure [17](#). The mean mass for the donor of M82 X-2 (Bachetti et al. [2022](#)) is $8\,M_\odot$. RX J0050.7-7316 (AX J0051-733; Coe & Orosz [2000](#)) seems to be the most debatable object. The best-fit mass ratio $q = 2.94$ by Coe & Orosz ([2000](#)) is located well below our predicted upper limit; but the spectrum of the donor star also supports a larger mass ratio $q = 6.66$ (Coe & Orosz [2000](#), and reference

Table 3
Observed IMXBs and Candidate IMXBs

Name1	Name2	$\frac{P_{orb}}{days}$	TypeM_X	SpTypeM_d	$\log_{10}\frac{L_X}{erg\,s^{-1}}$	$\sigma_{\log_{10}\frac{L_X}{erg\,s^{-1}}}$	Ecce	$q=\frac{M_d}{M_X}$	σ_q	$\frac{M_X}{M_\odot}$	$\sigma\frac{M_X}{M_\odot}$	$\frac{M_d}{M_\odot}$	$\sigma\frac{M_d}{M_\odot}$	Ref.
3A 1909+048	SS 433	13.100	BH	A4I-A8I	>37.30	...	...	≤1.67	−0.92	≥5–9	...	10.40	±2.10	1–3
3A 1909+048	SS 433	13.080	BH	A7I	...	...	...	2.86	$^{+1.60}_{-1.10}$	4.30	±0.80	12.30	±3.30	4
SAX J1819.3-2525	V4641 Sgr	2.817	BH	B9/3	39.23	...	...	0.45	±0.04	6.40	±0.60	2.90	±0.40	5
SAX J1819.3-2525	V4641 Sgr	2.817	BH	B9/3	39.46	2.30E-01	...	0.67	±0.04	9.61	$^{+2.08}_{-0.88}$	6.53	$^{+1.60}_{-1.03}$	6
V1033 Sco	GRO J1654–40	2.621	BH	F6/4	...	...	...	0.26	±0.04	5.40	±0.30	1.45	±0.35	7
V1033 Sco	GRO J1654–40	2.621	BH	F6/4	...	...	...	0.42	±0.03	6.59	±0.45	2.76	±0.33	8
BW Cir	GS 1354–6429	2.545	BH	G0-5/3	38.41	...	...	0.12	±0.02	≥7.83	±0.50	≥1.02	±0.17	9–10
IL Lup	4U 1543-47	1.116	BH	A2/5	39.56	...	...	0.29	$^{+0.21}_{-0.14}$	9.40	±2.00	2.70	±1.00	11-13
GRO J1716-24	V2293 Oph	0.613	BH	...	...	...	...	0.33	...	≥4.90	...	1.60	...	14
2S 1417-624	...	42.120	NS	B1Ve	>37.34	...	0.446	≥4.20	...	1.40	...	≥5.90	...	15–16
KS 1947+300	GRO J1948+32	40.415	NS	B0Ve	38.04	...	0.033	≥3.57	+3.57?	1.40	...	≥5.00?	+5.00?	17
AX J0049-729	RX J0049.1–7250	33.380	NS	B3Ve	37.54	...	0.400	5.36	±1.07	1.40	...	7.50	±1.50	18
4U 1901+03	...	22.580	NS	...	38.04	...	0.036	>3.21–4.29	...	1.40	...	≥4.50	+1.50	19
3A 1909+048	SS 433	13.100	NS?	pec	...	...	...	4.00	±1.18	0.80	±0.10	3.20	±0.40	20
SAX J2103.5+4545	...	12.680	NS	B0Ve	35.90	...	0.400	5.00	...	1.40	...	7.00	...	21
2A 1655+353	Her X-1	1.700	NS	A9-B	37.30	...	...	2.03	±0.42	0.98	±0.12	1.99	±0.14	22
RX J0050.7-7316	AX J0051-733	1.416	NS	...	36.30	...	...	6.66	±1.67	1.40	...	8.70	...	23
RX J0050.7-7316	AX J0051-733	1.416	NS	...	36.30	...	...	2.94	...	1.40	...	4.12	...	23
1WGA J0648.0-4419	HD 49798	1.550	NS	sdO6	32.00	...	...	1.17	±0.09	1.28	±0.05	1.50	±0.05	24–26
NGC 5907 ULX1	...	5.300	NS-ULXs	...	40.88	4.62E-01	...	2.86	±1.43	1.40	...	4.00	±2.00	27–28
M82 X-2	...	2.533	NS-ULXs	...	39.82	7.00E-03	≤0.003	≥3.71	+2	1.40	...	≥5.20	+2.80	29–30
M82 X-2	...	2.520	NS-ULXs	...	39.82	7.00E-03	...	3.93	±1.79	1.40	...	5.50	±2.50	31
M51 ULX-7	...	1.997	NS-ULXs	...	39.85	7.00E-02	≤0.220	≥5.71	...	1.40	...	≥8.00	...	32

Notes. Objects are selected from catalogs of LMXBs (Ritter & Kolb 2003; Liu et al. 2007), HMXBs (Liu et al. 2006), and a paper about ULXs (Misra et al. 2020).

References: (1) Cherepashchuk et al. (2019); (2) Middleton et al. (2021); (3) Waisberg et al. (2019); (4) Hillwig & Gies (2008); (5) MacDonald et al. (2014); (6) Orosz et al. (2001); (7) Beer & Podsiadlowski (2002); (8) Shahbaz (2003); (9) Casares et al. (2009); (10) Casares et al. (2004); (11) Orosz et al. (1998); (12) Orosz (2003); (13) Park et al. (2004); (14) Masetti et al. (1996); (15) Finger et al. (1996); (16) İnam et al. (2004); (17) Galloway et al. (2004); (18) Townsend et al. (2011); (19) Galloway et al. (2005); (20) D'Odorico et al. (1991); (21) Baykal et al. (2000); (22) Nagase (1989); (23) Coe & Orosz (2000); (24) Brooks et al. (2017); (25) Mereghetti et al. (2009); (26) Mereghetti et al. (2021); (27) Misra et al. (2020); (28) Israel et al. (2017); (29) Bachetti et al. (2014); (30) Bachetti et al. (2022); (31) Fragos et al. (2015); (32) Rodríguez Castillo et al. (2020).
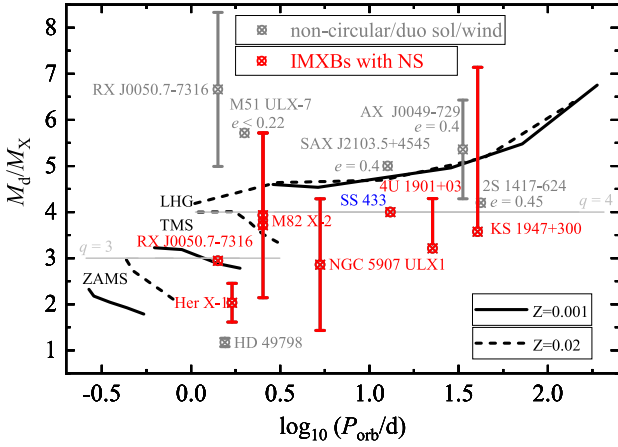
Figure 17. Mass ratio as a function of orbital period for IMXBs containing a NS accretor. Black solid ($Z = 0.001$) and dashed ($Z = 0.02$) lines show the mass ratio $M_d/M_X = \bar{q}_{ad}(M_d, R)$ where the radius R of the donor equals its Roche-lobe radius R_L for the given orbital period P_{orb}. From bottom to top, black solid and dashed lines are for donor stars on the ZAMS, TMS, and LHG. Red symbols are IMXBs with small eccentricities. These are located right below our predictions (black lines). Gray symbols are eccentric IMXBs, which cannot be constrained directly from our 1D model. The best-fit mass ratio of RX J0050.7-7316 fits better, but others suggest its orbital period might be around 150 days.
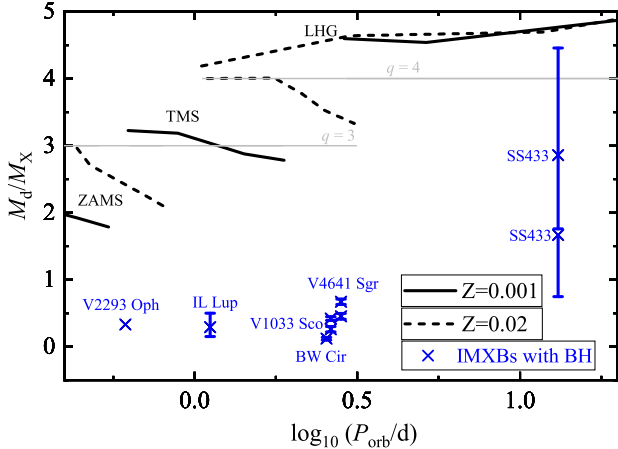
Figure 18. Similar to Figure 17 but for IMXBs containing a BH (blue cross).

therein). We suspect that the mass of a stripped star could be overestimated based on its spectrum if it is not in thermal equilibrium. Coe et al. (2005) and Schmidtke & Cowley (2005) argue that the observed period might actually be nonradial pulsation and the X-ray data suggest a much longer orbital period of 108 days (Laycock et al. 2005) or 185 days (Imanishi et al. 1999).

We have not considered eccentric orbits when we calculated critical mass ratios, which are derived on the assumption that $e = 0$. Thus, our results are not valid for eccentric IMXBs such as 2S 1417–624, AX J0049-729, SAX J2103.5+4545, and M51 ULX-7. Our critical mass ratios are given for IMXBs that initially formed and triggered RLOF. However, the mass ratios of observed IMXBs decrease gradually during the thermal timescale mass-transfer process. For IMXBs with a BH, most of these objects' mass ratios are reversed (less than 1) except SS 433. This is consistent with our expectation that a lower mass-transfer rate after the mass ratio reverse lasts a long time to be observed.

6.2. Max X-Ray Luminosities of Intermediate-mass X-Ray Binaries

The accretion luminosity of accreting BHs may be written as (Frank et al. 2002)

$$L_{acc} = 2\eta_{acc} GM_X \dot{M}_{acc}/R_*$$
$$= \eta_{acc} \dot{M}_{acc} c^2, \tag{16}$$

where the dimensionless parameter η_{acc} measures how efficiently the rest mass energy, c^2 per unit mass, of the accreted material is converted into radiation, and $R_* = 2GM_X/c^2$ defines the BH radius. The dimensionless efficiency parameter is generally taken to be $\eta_{acc} = 0.1$, but it could be up to $\eta_{acc} = 0.2$ or 0.4 for a 1.4 $M_\odot$ NS or a maximally rotating BH. The Eddington limit to accretion luminosity is (Frank et al. 2002)

$$L_{Edd} = 4\pi GM_X m_p c/\sigma_T$$
$$\approx 1.3 \times 10^{38}(M_X/M_\odot) \text{erg s}^{-1}, \tag{17}$$

where m_p is the proton mass and $\sigma_T = 6.7 \times 10^{-25}$ cm^2 is the Thomson cross section for fully ionized hydrogen. The corresponding Eddington limit to mass accretion rate (Misra et al. 2020) is

$$\dot{M}_{Edd} \approx 1.5 \times 10^{-8}(M_X/1.3M_\odot)M_\odot \text{ yr}^{-1}. \tag{18}$$

To explain the X-ray spectrum of IMXBs, the low/hard or high/soft states (Remillard & McClintock 2006), requires detailed accretion physics with disk formation, angular momentum transfer, magnetic fields, and energy dissipation (collisions of gas elements, shocks, viscous dissipation, etc.; Frank et al. 2002). However, the overall accretion energy of the compact accretor is generated by the material transferred from the donor star. Our predictions for the extremes of the X-ray luminosity are consistent with observed systems (Figure 19).

The thermal timescale mass-transfer rate (Paper I) of the donor star can be written as

$$\dot{M}_{KH}^d = M_d/\tau_{KH} = R_d L_d/GM_d, \tag{19}$$

where τ_{KH} is the Kelvin–Helmholtz timescale, and the nuclear as

$$\dot{M}_{nuc}^d = M_d/\tau_{nuc} = 1 \times 10^{-10}(L_d/L_\odot)M_\odot \text{ yr}^{-1}. \tag{20}$$

If the thermal (Equation (19)) or nuclear (Equation (20)) timescale mass-transfer rate exceeds that of the Eddington rate (Equation (18)), we assume the mass accretion rate is

$$\dot{M}_{acc} = \eta_d \dot{M}_{KH}^d, \text{ or}$$
$$= \eta_d \dot{M}_{nuc}^d, \tag{21}$$

with an efficiency $\eta_d = 0.1$. If the mass-transfer rate is smaller than the Eddington limit, we assume $\eta_d = 1.0$, and

$$L_{acc} = \eta_d \eta_{acc} \dot{M}_{KH}^d c^2, \text{ or}$$
$$= \eta_d \eta_{acc} \dot{M}_{nuc}^d c^2. \tag{22}$$

We use the observed IMXBs with available X-ray luminosity L_X and noneccentric orbit to constrain the efficiency parameters η_d and η_{acc}. Figure 19 shows that the upper tracks of the observed X-ray luminosity L_X are below $0.02\dot{M}_{KH}^d c^2$. So the peak X-ray luminosity is described well by nonconserved
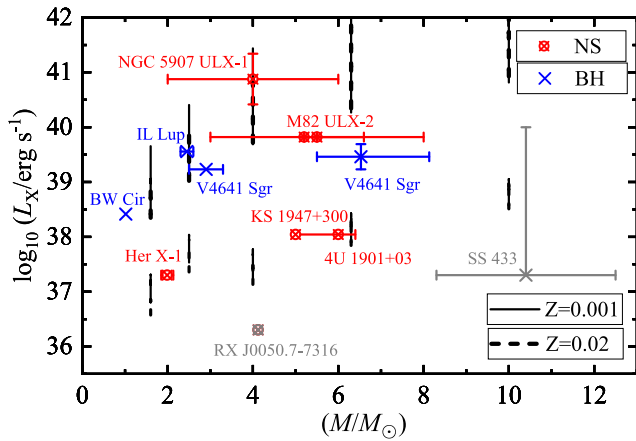
Figure 19. X-ray peak luminosity of IMXBs as a function of donor mass. Red and blue symbols indicate IMXBs with a NS or BH accretor. Black solid ($Z = 0.001$) and dashed ($Z = 0.02$) vertical lines are theoretical predictions. The masses of these black vertical lines are 1.6, 2.5, 4.0, 6.3, and 10.0 $M_\odot$, from left to right. According to the mass-transfer rate of the donor, there are two track zones. The upper tracks of L_X follow $0.02\dot{M}_{KH}^d c^2$ (nonconserved thermal timescale mass transfer and super-Eddington accretion), while the lower tracks obey $0.1\dot{M}_{nuc}^d c^2$ (conserved nuclear timescale mass transfer) or $0.01\dot{M}_{nuc}^d c^2$ (nonconserved nuclear timescale mass transfer and super-Eddington accretion). RX J0050.7-7316 is a problematic object, but see discussions in Section 6.1.

($\eta_d = 0.1$) thermal timescale mass transfer and super-Eddington accretion. The lower tracks of L_X are above $0.1\dot{M}_{nuc}^d c^2$ (conserved $\eta_d = 1.0$ nuclear timescale mass transfer) or $0.01\dot{M}_{nuc}^d c^2$ (nonconserved $\eta_d = 0.1$ nuclear timescale mass transfer and super-Eddington accretion).

The peak X-ray luminosity L_X of observed IMXBs spans over four orders of magnitude. From the point of the energy contribution from the donor star, we find the peak X-ray luminosity can be explained well by using thermal (upper tracks) or nuclear (lower tracks) timescale mass transfer. The upper tracks of L_X are derived from the nonconserved thermal timescale mass transfer, which is powered by a super-Eddington accretion. The lower tracks of L_X are calculated from nuclear timescale mass tranfer, which could be a conserved mass transfer ($M_d < 4\,M_\odot$) or a nonconserved ($M_d > 4\,M_\odot$) super-Eddington accretion. We simply assume the bolometric luminosity equals the X-ray luminosity. However, Middleton et al. (2021) determine an intrinsic X-ray luminosity $\geqslant 2 \times 10^{37}$ erg s^{-1} for SS 433. They infer that the hard X-ray emission from the inner regions is likely being scattered toward us by the walls of the wind cone. If viewed face-on, they infer an apparent luminosity $>1 \times 10^{39}$ erg s^{-1}. Furthermore, the optical/UV luminosity of SS 433 is in excess of 10^{40} erg s^{-1} (Waisberg et al. 2019). For super-Eddington accretion, it can be difficult to reliably relate $\dot{M}$ to L_X as the geometry of the accretion flow can introduce an isotropic in the radiation pattern. However, by observing changes in the P_{orb} of M82 X-2, Bachetti et al. (2022) were able to place independent constraints on $\dot{M}$. This could allow us to avoid any issues with accretion efficiency or beaming.

7. Summary

This study is an extension of a series of studies (Papers I, II, and III), which present systematically the critical mass ratios for dynamical timescale mass transfer over the span of donor star evolutionary states ($Z = 0.02$). Using $4\,M_\odot$ donor stars as

examples, we study the different responses of stars with metallicities $Z = 0.02$ and $Z = 0.001$, as well as their critical mass ratios. We present the critical mass ratios of IM stars with masses from 1.6 to 10.0 $M_\odot$ with $Z = 0.001$. Both a tabular form ($Z = 0.001$ only) and fitting formulae ($Z = 0.001$ and $Z = 0.02$) of the critical mass ratios are provided in this paper. For metal-poor MS and HG donor stars, we find the critical mass ratios are smaller than those of solar-metallicity stars at the same evolutionary stage. However, for metal-poor RGB/ AGB donor stars, we find the critical mass ratios are larger than those of the solar-metallicity stars with the same radii. Hence, metallicity has an important impact on the thresholds for dynamical timescale mass transfer which leads to the common-envelope evolution. We apply our results to 17 observed IMXBs with available mass ratios and orbital periods. We find our prediction constrains well the observed IMXBs that undergo thermal or nuclear timescale mass transfer. We give a prediction of the upper and lower tracks to the X-ray luminosities of IMXBs as a function of the donor mass and the mass-transfer timescale. This prediction based on a donor star might be a helpful complement to accretion disk physics.

ORCID iDs

Hongwei Ge https://orcid.org/0000-0002-6398-0195
Christopher A Tout https://orcid.org/0000-0002-1556-9449
Xuefei Chen https://orcid.org/0000-0001-5284-8001
Arnab Sarkar https://orcid.org/0000-0002-1455-2784
Dominic J Walton https://orcid.org/0000-0001-5819-3552
Zhanwen Han https://orcid.org/0000-0001-9204-7778

References

Abbott, R., Abbott, T. D., Abraham, S., et al. 2021, PhRvX, 11, 021053
Akerman, C. J., Carigi, L., Nissen, P. E., Pettini, M., & Asplund, M. 2004, A&A, 414, 931
Asplund, M., Grevesse, N., Sauval, A. J., & Scott, P. 2009, ARA&A, 47, 481
Bachetti, M., Harrison, F. A., Walton, D. J., et al. 2014, Natur, 514, 202
Bachetti, M., Heida, M., Maccarone, T., et al. 2022, ApJ, 937, 125
Baykal, A., Stark, M. J., & Swank, J. 2000, ApJL, 544, L129
Beer, M. E., & Podsiadlowski, P. 2002, MNRAS, 331, 351
Belczynski, K., Dominik, M., Bulik, T., et al. 2010, ApJL, 715, L138
Briel, M. M., Stevance, H. F., & Eldridge, J. J. 2022, MNRAS, in press
Brooks, J., Kupfer, T., & Bildsten, L. 2017, ApJ, 847, 78
Casares, J., Orosz, J. A., Zurita, C., et al. 2009, ApJS, 181, 238
Casares, J., Zurita, C., Shahbaz, T., Charles, P. A., & Fender, R. P. 2004, ApJL, 613, L133
Cherepashchuk, A. M., Postnov, K. A., & Belinski, A. A. 2019, MNRAS, 485, 2638
Coe, M. J., Negueruela, I., & McBride, V. A. 2005, MNRAS, 362, 952
Coe, M. J., & Orosz, J. A. 2000, MNRAS, 311, 169
Corral-Santana, J. M., Casares, J., Muñoz-Darias, T., et al. 2016, A&A, 587, A61

de Mink, S. E., & Mandel, I. 2016, MNRAS, 460, 3545
D'Odorico, S., Oosterloo, T., Zwitter, T., & Calvani, M. 1991, Natur, 353, 329
Dorozsmai, A., & Toonen, S. 2022, arXiv:2207.08837
Duchêne, G., & Kraus, A. 2013, ARA&A, 51, 269
Eggleton, P. P. 1983, ApJ, 268, 368
Finger, M. H., Wilson, R. B., & Chakrabarty, D. 1996, A&AS, 120, 209
Fragos, T., Linden, T., Kalogera, V., & Sklias, P. 2015, ApJL, 802, L5
Frank, J., King, A., & Raine, D. J. 2002, Accretion Power in Astrophysics: Third Edition (Cambridge: Cambridge Univ. Press)
Gallegos-Garcia, M., Berry, C. P. L., Marchant, P., & Kalogera, V. 2021, ApJ, 922, 110
Galloway, D. K., Morgan, E. H., & Levine, A. M. 2004, ApJ, 613, 1164
Galloway, D. K., Wang, Z., & Morgan, E. H. 2005, ApJ, 635, 1217
Ge, H., Hjellming, M. S., Webbink, R. F., Chen, X., & Han, Z. 2010, ApJ, 717, 724
Ge, H., Webbink, R. F., Chen, X., & Han, Z. 2013, Feeding Compact Objects: Accretion on All Scales, ed. C. M. Zhang et al., Vol. 290 (Cambridge: Cambridge Univ. Press), 213
Ge, H., Webbink, R. F., Chen, X., & Han, Z. 2015, ApJ, 812, 40
Ge, H., Webbink, R. F., Chen, X., & Han, Z. 2020a, ApJ, 899, 132
Ge, H., Webbink, R. F., & Han, Z. 2020b, ApJS, 249, 9
Hillwig, T. C., & Gies, D. R. 2008, ApJL, 676, L37
Hjellming, M. S. 1989, Urbana-Champaign, PhD thesis, University of Illinois, Urbana-Champaign
Hjellming, M. S., & Webbink, R. F. 1987, ApJ, 318, 794
Iben, I. J., & Rood, R. T. 1970, ApJ, 161, 587
Imanishi, K., Yokogawa, J., Tsujimoto, M., & Koyama, K. 1999, PASJ, 51, L15
İnam, S. Ç., Baykal, A., Matthew Scott, D., Finger, M., & Swank, J. 2004, MNRAS, 349, 173
Inayoshi, K., Hirai, R., Kinugawa, T., & Hotokezaka, K. 2017, MNRAS, 468, 5020
Israel, G. L., Belfiore, A., Stella, L., et al. 2017, Sci, 355, 817
Kalogera, V., & Webbink, R. F. 1996, ApJ, 458, 301
King, A. R., & Ritter, H. 1999, MNRAS, 309, 253
Klencki, J., Istrate, A., Nelemans, G., & Pols, O. 2022, A&A, 662, A56
Klencki, J., Nelemans, G., Istrate, A. G., & Pols, O. 2020, A&A, 638, A55
Laycock, S., Corbet, R. H. D., Coe, M. J., et al. 2005, ApJS, 161, 96
Li, H., Tan, K., & Zhao, G. 2018, ApJS, 238, 16
Li, J., Li, J., Liu, C., et al. 2022, ApJ, 933, 119
Li, X.-D. 2020, RAA, 20, 162
Liu, Q. Z., van Paradijs, J., & van den Heuvel, E. P. J. 2006, A&A, 455, 1165
Liu, Q. Z., van Paradijs, J., & van den Heuvel, E. P. J. 2007, A&A, 469, 807
MacDonald, R. K. D., Bailyn, C. D., Buxton, M., et al. 2014, ApJ, 784, 2
Mandel, I., & de Mink, S. E. 2016, MNRAS, 458, 2634
Marchant, P., Pappas, K. M. W., Gallegos-Garcia, M., et al. 2021, A&A, 650, A107
Masetti, N., Bianchini, A., Bonibaker, J., della Valle, M., & Vio, R. 1996, A&A, 314, 123
McWilliam, A., Preston, G. W., Sneden, C., & Shectman, S. 1995, AJ, 109, 2736
Mereghetti, S., Pintore, F., Rauch, T., et al. 2021, MNRAS, 504, 920
Mereghetti, S., Tiengo, A., Esposito, P., et al. 2009, Sci, 325, 1222

Middleton, M. J., Walton, D. J., Alston, W., et al. 2021, MNRAS, 506, 1045
Misra, D., Fragos, T., Tauris, T. M., Zapartas, E., & Aguilera-Dena, D. R. 2020, A&A, 642, A174
Moe, M., & Di Stefano, R. 2017, ApJS, 230, 15
Nagase, F. 1989, PASJ, 41, 1
Orosz, J. A. 2003, A Massive Star Odyssey: From Main Sequence to Supernova, ed. K. van der Hucht, A. Herrero, & C. Esteban, Vol. 212 (San Francisco, CA: ASP), 365
Orosz, J. A., Jain, R. K., Bailyn, C. D., McClintock, J. E., & Remillard, R. A. 1998, ApJ, 499, 375
Orosz, J. A., Kuulkers, E., van der Klis, M., et al. 2001, ApJ, 555, 489
Paczynski, B. 1976, Structure and Evolution of Close Binary Systems, ed. P. Eggleton, S. Mitton, & J. Whelan, Vol. 73 (Dordrecht: D. Reidel Publishing Co.), 75
Park, S. Q., Miller, J. M., McClintock, J. E., et al. 2004, ApJ, 610, 378
Pavlovskii, K., Ivanova, N., Belczynski, K., & Van, K. X. 2017, MNRAS, 465, 2092
Podsiadlowski, P., & Rappaport, S. 2000, ApJ, 529, 946
Podsiadlowski, P., Rappaport, S., & Pfahl, E. D. 2002, ApJ, 565, 1107
Pols, O. 2011, Stellar Structure and Evolution (Nijmegen: Astronomical Institute Utrecht), https://www.astro.ru.nl/~onnop/education/stev_utrecht_notes/
Preston, G. W., & Sneden, C. 2000, AJ, 120, 1014
Remillard, R. A., & McClintock, J. E. 2006, ARA&A, 44, 49
Ritter, H., & Kolb, U. 2003, A&A, 404, 301
Rodríguez Castillo, G. A., Israel, G. L., Belfiore, A., et al. 2020, ApJ, 895, 60
Ryan, S. G., Norris, J. E., & Beers, T. C. 1996, ApJ, 471, 254
Sana, H., de Mink, S. E., de Koter, A., et al. 2012, Sci, 337, 444
Schmidtke, P. C., & Cowley, A. P. 2005, AJ, 130, 2220
Shahbaz, T. 2003, MNRAS, 339, 1031
Shao, Y., & Li, X.-D. 2012, ApJ, 756, 85
Sneden, C. 1973, ApJ, 184, 839
Sneden, C. 1974, ApJ, 189, 493
Tauris, T. M., & van den Heuvel, E. P. J. 2006, Compact Stellar X-ray Sources, Vol. 39 (Cambridge: Cambridge Univ. Press), 623
Tauris, T. M., van den Heuvel, E. P. J., & Savonije, G. J. 2000, ApJL, 530, L93
Temmink, K. D., Pols, O. R., Justham, S., Istrate, A. G., & Toonen, S. 2023, A&A, 669, A45
Tetarenko, B. E., Sivakoff, G. R., Heinke, C. O., & Gladstone, J. C. 2016, ApJS, 222, 15
Townsend, L. J., Coe, M. J., Corbet, R. H. D., & Hill, A. B. 2011, MNRAS, 416, 1556
Vink, J. S., Higgins, E. R., Sander, A. A. C., & Sabhahit, G. N. 2021, MNRAS, 504, 146
Waisberg, I., Dexter, J., Olivier-Petrucci, P., Dubus, G., & Perraut, K. 2019, A&A, 624, A127
Walton, D. J., Mackenzie, A. D. A., Gully, H., et al. 2022, MNRAS, 509, 1587
Wu, Y., Xiang, M., Chen, Y., et al. 2021, MNRAS, 501, 4917
Yan, Z., Jerabkova, T., & Kroupa, P. 2020, A&A, 637, A68
Yoon, S. C., & Langer, N. 2005, A&A, 443, 643
Zampieri, L., & Roberts, T. P. 2009, MNRAS, 400, 677
Zhao, G., Chen, Y.-Q., Shi, J.-R., et al. 2006, ChJAA, 6, 265